Gravity-driven membrane filtration as pretreatment for seawater reverse osmosis: Linking biofouling layer morphology with flux stabilization

Ebrahim Akhondi [a], Bing Wu [a,*], Shuyang Sun [b,c], Brigit Marxer [d], Weikang Lim [a], Jun Gu [e], Linbo Liu [e], Michael Burkhardt [d], Diane McDougald [b,c], Wouter Pronk [f], Anthony G. Fane [a,g]

[a] Singapore Membrane Technology Centre, Nanyang Environment and Water Research Institute, Nanyang Technological University, 1 Cleantech Loop, CleanTech One #06-08, Singapore 637141, Singapore
[b] Singapore Centre on Environmental Life Sciences Engineering, Nanyang Technological University, 60 Nanyang Drive, Singapore 637551, Singapore
[c] Centre for Marine Bio-Innovation, The University of New South Wales, Sydney, NSW 2052, Australia
[d] Institute of Environmental and Process Engineering, HSR University of Applied Sciences Rapperswil, Oberseestrasse 10, 8640 Rapperswil, Switzerland
[e] School of Electrical & Electronic Engineering, Nanyang Technological University, 50 Nanyang Avenue, Singapore 639798, Singapore
[f] Eawag, Swiss Federal Institute of Aquatic Science and Technology, Ueberlandstrasse 133, 8600 Duebendorf, Switzerland
[g] School of Civil and Environmental Engineering, Nanyang Technological University, 50 Nanyang Avenue, Singapore 639798, Singapore

ARTICLE INFO

ABSTRACT

In this study gravity-driven membrane (GDM) ultrafiltration is investigated for the pretreatment of seawater before reverse osmosis (RO). The impacts of temperature (21 ± 1 and 29 ± 1 °C) and hydrostatic pressure (40 and 100 mbar) on dynamic flux development and biofouling layer structure were studied. The data suggested pore constriction fouling was predominant at the early stage of filtration, during which the hydrostatic pressure and temperature had negligible effects on permeate flux. With extended filtration time, cake layer fouling played a major role, during which higher hydrostatic pressure and temperature improved permeate flux. The permeate flux stabilized in a range of 3.6 L/m² h (21 ± 1 °C, 40 mbar) to 7.3 L/m² h (29 ± 1 °C, 100 mbar) after slight fluctuations and remained constant for the duration of the experiments (almost 3 months). An increase in biofouling layer thickness and a variable biofouling layer structure were observed over time by optical coherence tomography and confocal laser scanning microscopy. The presence of eukaryotic organisms in the biofouling layer was observed by light microscopy and the microbial community structure of the biofouling layer was analyzed by sequences of 16S rRNA genes. The magnitude of permeate flux was associated with the combined effect of the biofouling layer thickness and structure. Changes in the biofouling layer structure were attributed to

(1) the movement and predation behaviour of the eukaryotic organisms which increased the heterogeneous nature of the biofouling layer; (2) the bacterial debris generated by eukaryotic predation activity which reduced porosity; (3) significant shifts of the dominant bacterial species over time that may have influenced the biofouling layer structure. As expected, most of the particles and colloids in the feed seawater were removed by the GDM process, which led to a lower RO fouling potential. However, the dissolved organic carbon in the permeate was not be reduced, possibly because some microbial species (e.g. algae) could convert CO_2 into organic substances. To further improve the removal efficiency of the organic carbon, combining carrier biofilm processes with a submerged GDM filtration system is proposed.

1. Introduction

Reverse osmosis (RO) has been widely implemented for seawater desalination. Due to the presence of particulate, colloidal, dissolved organic and inorganic matters, and biofilm-forming microorganisms in the feed seawater, the RO membranes potentially suffer particulate fouling, scaling, organic fouling, and biofouling (Bae et al., 2011; Sutzkover-Gutman and Hasson, 2010). To improve process efficiency and lessen RO membrane fouling, the seawater feed needs to be pretreated before the RO process. Conventional pretreatment processes such as coagulation, dissolved air flotation, and media filtration have been shown to mitigate RO membrane fouling (Bonnelye et al., 2004; Voutchkov, 2010). Recently, membrane-based pretreatment processes, e.g., microfiltration (MF) (Bae et al., 2011), ultrafiltration (UF) (Huang et al., 2011), and nanofiltration (NF) have been increasingly considered to replace the conventional pretreatment processes as they are chemical-free (except membrane cleaning chemicals), space saving and result in superior permeate quality (Pearce, 2008).

The benefits of UF/MF membrane pretreatment processes are, however, lessened by their high energy demand (Knops et al., 2007), which is mainly due to membrane fouling control strategies (such as cross-flow, backwashing, and air scouring etc.) (Akhondi et al., 2014). Elimelech and Phillip (2011) emphasized that the energy demand for the pretreatment of raw seawater accounts for the majority of the total energy used for intake, pretreatment, posttreatment, and brine discharge stages. Moreover, Voutchkov (2010) stated that when pretreating seawater by UF membranes during an algal bloom, the seawater filtrate could increase biofouling on RO membranes if the driving pressure was great enough to rupture the algal cells (a limiting pressure of >0.4 bar was suggested). Thus, there is an incentive to develop low-energy membrane-based RO pretreatment processes delivering beach-well quality permeate. Such pretreatment could potentially contribute more to the overall process energy efficiency than the remaining incremental opportunities for the RO process.

Gravity-driven membrane (GDM) filtration, initially developed by researchers from the Swiss Federal Institute of Aquatic Science and Technology (Eawag), has been used to treat a broad range of surface waters with differing levels of natural organic matter (NOM) and inorganic components, as well as diluted wastewaters (Derlon et al., 2013, 2012; Peter-Varbanets et al., 2012, 2010, 2011). In a dead-end filtration mode, GDM filtration uses gravity to move the water across the membrane. Results have shown that a stable flux (2–20 L/m^2 h, depending on NOM concentration, temperature, oxygen content, and the microbial community in the fouling layer) can be achieved without the need for backwashing or flushing when the hydrostatic pressure is approximately 40–60 mbar. Flux stabilization is attributed to the formation of a porous, heterogeneous cake (i.e., biofouling layer) on the UF membrane, which is the result of deposition of non-biodegradable substances and microorganisms, combined with bacterial activity and predation by eukaryotic organisms (e.g., heterotrophic protists) (Derlon et al., 2013, 2012; Peter-Varbanets et al., 2011).

Due to increased interest in low energy and chemical-free processes for pretreatment of seawater for RO, GDM filtration is potentially attractive. Compared to the energy consumption for the conventional UF/MF processes for RO pretreatment (0.1–0.3 kWh/m^3 treated water) (Pearce, 2008), GDM filtration requires negligible energy input for the generation of the head, i.e. approximately 0.01 kWh/m^3 treated water. Chemical use for membrane cleaning is also negligibly small.

The aim of this study is to evaluate GDM filtration as an RO pretreatment process. Flux and membrane fouling was investigated during dead-end, low-pressure ultrafiltration of seawater. The influences of temperature and the hydrostatic driving force on system performance were investigated. In addition, the dynamic biofouling layer morphology, structural changes, and microbial community composition of the biofouling layer were monitored and the permeate quality was examined.

2. Materials and methods

2.1. Seawater

Raw seawater was collected from West Coast Park beach, Singapore, from September to December 2013 and screened

through 100 μm mesh filters (Millipore, USA). To ensure a constant temperature, the screened seawater (herein defined as feed seawater) was incubated at the same temperature as the setup for a few hours prior to addition to the system.

2.2. Experimental setup

Two identical gravity-driven UF systems were employed to conduct experiments at 21 ± 1 and 29 ± 1 °C in parallel, as shown in Fig. 1a. The setup was located inside a dark container and all filtration cells, tubings, and tanks were covered by aluminium foil in order to prevent algal growth. In each setup, feed seawater was added to the storage tank periodically, and pumped to the feed tank. The water level in the feed tank was kept constant by overflow, which was connected to the storage tank. The membrane filtration cells were connected by silicon tubing to the feed tank and placed on horizontal stages (Fig. 1a). For each temperature, three membrane filtration cells were operated at a hydrostatic pressure of 40 mbar and three cells at 100 mbar. The permeates of two modules of the triplicates were collected in a separate plastic bottle and weighed using an electric scale (OHAUS, USA) daily. One of the permeate bottles of the triplicates was weighed by an electric scale (OHAUS, USA) every 10 min, which was connected to a computer equipped with a data-logging software.

The membrane filtration cells consisted of bottom (permeate side) and top (feed side) parts and were made of anodized aluminium, which were assembled as shown in Fig. 1b. The top had a glass window which allowed observation of the biofouling layer morphology. A flat sheet polysulfone (Microdyn Nadir, Germany) membrane (a nominal cut-off of 100 kDa) with a membrane area of 0.00231 m^2 was placed on top of the polycarbonate spacer between the two parts of the cell. The clean membranes were soaked in distilled water for 24 h to remove impurities before use.

2.3. Flux and hydraulic resistance

The permeate flux (L/m^2 h, LMH) was calculated by dividing the weight of permeate generated during a certain period of filtration by the membrane area. The measured flux (J_T) at temperature T was normalized to 20 °C using Eq. (1):

$$J_{20°C} = \frac{J_T \cdot \mu_T}{\mu_{20°C}} \qquad (1)$$

where $J_{20°C}$, J_T, $\mu_{20°C}$, and μ_T represents the corrected permeate flux at 20 °C, the measured permeate flux at temperature T, the water viscosity at 20 °C and the water viscosity at operational temperature T, respectively. The viscosity μ_T was calculated according to an empirical equation according to US EPA (EPA, 2005),

$$\mu_T = 1.784 - (0.0575 \cdot T) + (0.0011 \cdot T^2) - (10^{-5} \cdot T^3) \qquad (2)$$

The total hydraulic resistance (m^{-1}, R) was calculate based on Darcy's law $R_{total} = TMP/(\mu_T J_T)$, in which μ_T is the permeate viscosity at temperature T, J_T is the measured permeate flux at temperature T and TMP is the transmembrane pressure (i.e., hydrostatic pressure). The clean membrane resistance (R_m) was measured using distilled water before seawater was fed into the system. The fouling resistance (including biofilm cake layer resistance and irreversible resistance) is obtained by subtracting the clean membrane resistance (R_m) from total hydraulic resistance (R_{total}).

2.4. Biofouling layer morphology observation

2.4.1. Optical coherence tomography (OCT)
A 1-μm resolution optical coherence tomography (μOCT) (Liu et al., 2011) was employed as a non-invasive approach to investigate the development of the in situ biofouling layer structure at the meso-scale. Periodically, the membrane filtration cell was carefully removed from the GDM system after the outlets of the filtration cell and GDM system were clamped. Following examination by μOCT, the filtration cell was returned to the GDM system and the filtration experiment was continued.

The μOCT utilizes a supercontinuum broadband light source (SuperK EXR-1, NKT Photonics, Denmark) to achieve a lateral resolution of ~2 μm and axial resolution of ~1.2 μm in water. The OCT images were collected through the cover glass window of the filtration cell. The cross-sectional images of the membrane and the biofouling layer were recorded at an A-line rate of 10,240 Hz and 20 frames per second with 512 A-lines per frame. The three dimensional images were also acquired with a sample size of 0.5 mm × 0.5 mm × 0.5 mm. For each sample, two randomly selected regions were imaged.
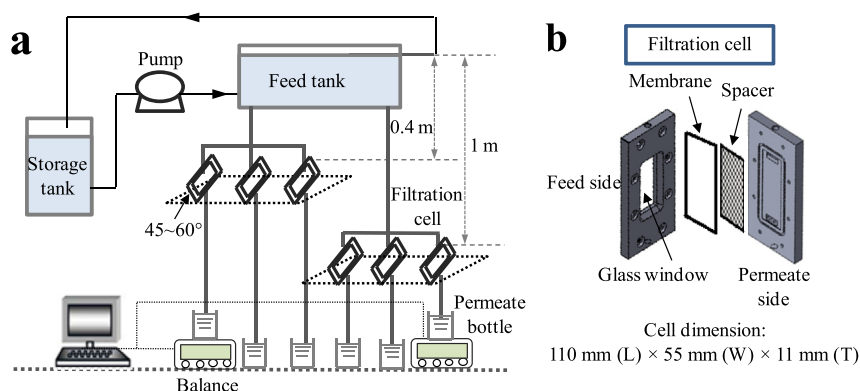

Fig. 1 – **A schematic describing gravity-driven UF filtration processes (a) and details of filtration cell (b).**

The biofouling layer thickness was calculated using the ImageJ software (NIH, USA). In brief, the image (video format) taken by OCT was exported to ImageJ. By adjusting the threshold value, only the biofouling layer above the membrane surface was selected. The pixel number from the membrane surface to the top of biofouling layer was measured. As each pixel corresponds to a certain length (in micron), the local biofouling layer thickness could be calculated. The physical properties of the biofouling layer such as mean biofouling layer thickness ($\acute{Z}$ in μm), absolute roughness coefficient (R_a in μm) and relative roughness coefficient (R'_a) were calculated according to the following equations (Derlon et al., 2012):

$$\acute{Z} = \frac{1}{n} \sum_{i=1}^{n} Z_i \tag{3}$$

$$R_a = \frac{1}{n} \sum_{i=1}^{n} \left(\left| Z_i - \acute{Z} \right| \right) \tag{4}$$

$$R'_a = \frac{1}{n} \sum_{i=1}^{n} \left(\frac{\left| Z_i - \acute{Z} \right|}{\acute{Z}} \right) \tag{5}$$

where n is the number of thickness measurements and Z_i is the local biofouling layer thickness (μm).

2.4.2. Direct observation of eukaryotic protists

The movement behaviour of eukaryotic protists inside the membrane filtration cell was directly observed through the cover glass window by an optical microscope (Axio Imager, Zeiss, Germany) under $200\times$ magnification.

2.4.3. Confocal laser scanning microscopy (CLSM)

After the membrane was removed from the membrane filtration cell for autopsy, a piece of membrane (0.5 cm × 0.5 cm) was cut from the membrane sample and stained with the LIVE/DEAD® BacLight™ bacterial viability kit (Molecular Probes, USA) following the manufacture's specifications. The morphology of the biofouling layer was observed and recorded by a CLSM (LSM780, Zeiss, Germany) under $400\times$ magnification. The live bacteria with intact plasma membranes were stained with a green fluorescent dye, SYTO 9, and the dead bacteria with compromised membranes were stained with a red fluorescent dye, propidium iodide. The biovolume, mean biofouling layer thickness, and porosity were obtained from the 3D images using IMARIS software (Bitplane, Switzerland).

2.5. Biofouling layer microbial community analysis

The biofouling layer was mechanically removed from the membrane and suspended in 5 mL of sterile artificial seawater. The genomic DNA of the microbial community in the biofouling layer was extracted by FastDNA® SPIN kit (MP Biomedicals, USA). The variable V1–V3 region of the 16S rRNA gene was sequenced by Illumina (MrDNA, USA). Sequencing results were analysed by QIIME software using the standard de novo operational taxonomic unit (OTU) approach. Due to the limited amount of eukaryotic DNA extracted from the biofouling layer, the analysis of the eukaryotic community composition was not performed.

2.6. Feed and permeate seawater characterization

The RO fouling potentials of the feed and permeate seawater were evaluated by silt density index (SDI) and modified fouling index (MFI). In order to collect the required amount of permeate for the test, a lab-scale submerged GDM system was setup in parallel at 21 ± 1 °C (Fig. S1 in the Supplementary data). The feed and permeate seawater were sampled when the permeate flux of the GDM system stabilized. Determination of the SDI is based on measuring the rate at which a membrane filter having 0.45 μm pores becomes plugged at a constant pressure (2.07 bar). The filtration time was fixed at 5 min (i.e., SDI_5) and the SDI_5 was calculated from the equation below:

$$SDI_5 = \left[(1 - t_i/t_f)/5 \right] \times 100 \tag{6}$$

Where t_i is the initial time to filter 500 ml seawater and t_f the final time after the filtration was performed for 5 min. This means for high fouling potential, ($t_f \gg t_i$), the SDI_5 approaches 20.

The MFI was determined using the same equipment and procedure used for the SDI. The MFI is defined as the gradient of the linear region of the plot of t/V versus V from the general constant pressure filtration equation (Boerlage et al., 1998; Schippers and Verdouw, 1980).

$$\frac{t}{V} = a + MFI \times V \tag{7}$$

Where t is filtration time, V is the filtrate volume, and a is the intercept constant.

The turbidity of the feed and permeate seawater were tested using a turbidity meter (Hach, USA). The total organic carbon (TOC) of the feed seawater and permeate seawater were monitored using a TOC analyzer (Shimadzu, Japan). The pH and conductivity of the feed and permeate water were determined by a pH/conductivity meter (Mettler Toledo, Switerzland). The dissolved oxygen (DO) in the feed tank was determined by a DO meter (YSI, USA). Selected cations in the feed and permeate water were analyzed by an inductively coupled plasma-optical emission spectrometry (ICP-OES, PerkinElmer, USA).

The polysaccharide content of the seawater was measured according to the method described by Dubois et al. (1956). Transparent exopolymer (TEP) content was estimated based on the method first introduced by Passow and Alldredge (1995). The sample was filtered through a polycarbonate filter (Millipore, USA) with a pore size of 0.1 μm, therefore we are reporting TEP > 0.1 μm. Size-exclusion chromatography, in combination with organic carbon and nitrogen detection (LC-OCD-OND) was used to quantify the major soluble organic fractions with different sizes and chemical functions in the feed and permeate waters (after being filtered through a 0.45 μm hydrophilic filter) (Huber et al., 2011). On-line purified mobile phase was delivered by an HPLC pump (S-100, Knauer, Berlin, Germany) at a flow rate of 1.1 mL/min to the chromatographic column (TSK HW 50S, 3000 theoretical plates, Toso, Japan). The sample from an autosampler (MLE, Dresden,

Germany) was mixed with the mobile phase prior to the column. The first detector after chromatographic separation was a non-destructive, fixed wavelength UV-detector (UVD 254 nm, type S-200, Knauer, Berlin, Germany) for analyzing organic carbon. For nitrogen detection, a side stream was diverted after UVD with a restricted flow rate 0.1 mL/min (back pressure-driven).

3. Results

3.1. Flux stabilization

The filtration cells with flat-sheet membranes were operated in a dead-end mode without cross-flow, backflushing or cleaning, at operating temperatures of 21 ± 1 °C and 29 ± 1 °C with gravitational TMPs of 40 and 100 mbar, respectively (Fig. 1). Under each condition, three filtration cells were operated in parallel and the measured permeate weights were repeatable. Fig. 2a shows the flux over the filtration time at different operating temperatures and hydrostatic pressures. It was found that the time-dependent flux profiles followed

similar four-stage patterns within the applied operation temperature and pressure.

During the first few days, the flux dropped considerably from ~60 LMH (data not shown in Fig. 2a) to ~5 LMH (Phase I). There was almost no difference in permeate flux for the various operating conditions. Similar results were reported by Peter-Varbanets et al. (2010, 2011, 2012) during the initial filtration of river water, lake water, and diluted wastewater using the GDM filtration technique. Following the first phase, the flux was observed to increase slightly (from ~5 LMH to ~6—10 LMH) (Phase II) over 5—7 days. The flux recovery was more obvious for the filtration cells operated at the higher temperature (29 ± 1 °C) or the higher hydrostatic pressure (100 mbar) in comparison to those at 21 ± 1 °C or 40 mbar respectively. After the flux recovery stage, the flux slowly declined (Phase III). Relatively stable fluxes were achieved by days 50—60 (Phase IV), and the stabilized fluxes were maintained until the end of the experiment (~105 days) for all conditions.

The experimental results summarized in Table 1 indicate that the level of flux stabilization depended on the operating temperature and hydrostatic pressure. The stabilized flux of the membranes operated at 29 ± 1 °C was almost 1.6-fold the flux at 21 ± 1 °C. In contrast to the results reported by Peter—Varbanets et al. for freshwater (Peter-Varbanets et al., 2010), the hydrostatic pressure was found to influence the stable flux of seawater filtration. As shown in Table 1, a higher hydrostatic pressure resulted in an increased stable flux: When the hydrostatic pressure was elevated from 40 to 100 mbar, the stable flux increased by 1 LMH and 1.6 LMH for 21 ± 1 °C and 29 ± 1 °C, respectively. This suggests that the extent of the stable flux improvement depended on temperature. To make a fair comparison, the corrected flux at 20 °C was calculated based on the measured flux (Table 1). These results also indicate that the higher temperature and hydrostatic pressure improved the flux.

The fouling (including biofilm cake layer fouling and irreversible fouling) resistances were calculated accordingly, and the trends of the fouling resistance with collected permeate volume under various operating conditions are presented in Fig. 2b. It can be noted that the GDM filtration was continuously operated without any flushing or backwashing and, at certain times of operation, it was necessary to remove the membranes from the filtration cell for examination of the biofilm morphology. Therefore, the individual dynamic cake layer fouling and irreversible fouling resistance could not be monitored in this study.

Similar to the flux profiles, the total fouling resistances developed with a four-stage trend (Fig. 2b). The initial fouling resistance (Phase I) was almost independent of the hydrostatic pressure and temperature. With increasing permeate productivity, the hydrostatic pressure and temperature appeared to have impacts on the fouling resistance. i.e., higher hydrostatic pressure or lower temperature induced more fouling resistance. The membrane fouling resistances during the stabilization period (Phase IV) shown in Table 1 indicate that when the hydrostatic pressure increased from 40 to 100 mbar, the fouling resistance almost doubled at both temperatures tested. This corresponds with a previous GDM study by Peter-Varbanets et al. (2010), where it was found that
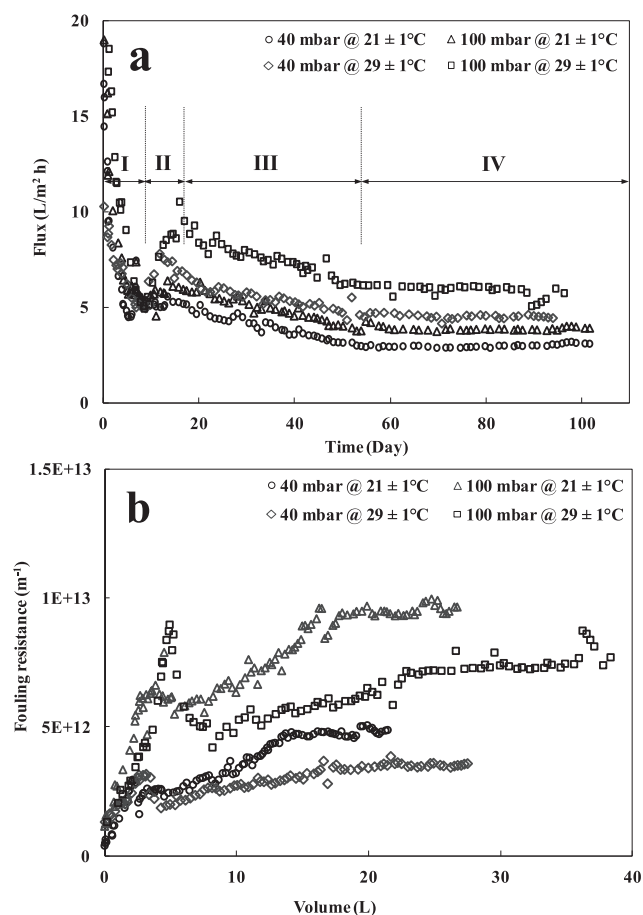
Fig. 2 — Permeate flux profiles (a) and fouling resistance profiles (b) of the membranes operated at different temperatures and filtration pressures (Note: Under each condition, the three parallel filtration cells had similar permeate weights, thus, a set of data were presented in the figure).

Table 1 – Effect of temperature and hydrostatic pressure on stabilized measured flux, corrected flux and fouling resistance ($n = 25$).				
Temperature	21 ± 1 °C		29 ± 1 °C	
Hydrostatic pressure	40 mbar	100 mbar	40 mbar	100 mbar
Measured flux (LMH)	3.6 ± 0.1	4.6 ± 0.2	5.7 ± 0.3	7.3 ± 0.4
Corrected flux at 20 °C (LMH)	3.4 ± 0.1	4.4 ± 0.2	4.6 ± 0.3	5.9 ± 0.4
Fouling resistance ($\times 10^{12}$ m^{-1})	4.8 ± 0.1	9.5 ± 0.2	3.6 ± 0.3	7.5 ± 0.4
Note: The presented data is calculated by averaging the measured data during stabilization period (Phase IV, Day 60 to Day 100).				

the fouling resistance at 150 mbar was a 2–3 factor higher than at 40 mbar. When the operating temperature varied from 21 ± 1 °C to 29 ± 1 °C, the fouling resistance was reduced by 25% (at 40 mbar) and 21% (at 100 mbar) respectively. This suggested that the hydrostatic pressure had a predominant role in determining the fouling resistance.

3.2. Biofouling layer morphology and microbial community

The meso-scale structure of the biofouling layer on the membrane over time was monitored in situ using a desktop μOCT system. Fig. 3 depicts the OCT images of the biofouling layers where the filtration cell was operated at 21 ± 1 °C and 40 mbar (the OCT images of the formed biofouling layers under the other conditions are presented in Figs. S2–S4). At the early stage of filtration (Day 0–7), a relatively thin biofouling layer was observed on the membrane surface. Under the dead-end filtration conditions, the non-dissolved and colloidal material in the feed seawater was retained and accumulated on the membrane, including bacteria, organic aggregated colloidal material, and particulate organic and inorganic material. The retained organic substances on the membrane can facilitate bacterial growth. With extended filtration time, the biofouling layer became thicker, more heterogeneous and porous.

To further quantify the OCT images and illustrate the biofouling layer development on the membrane, image analysis was applied to calculate the mean biofouling layer thicknesses, relative and absolute roughness coefficients, as depicted in Fig. 4. Overall, the effects of temperature and hydrostatic pressure on thickness, the absolute and relative roughness coefficients were not evident. The thickness of the biofouling layer increased nearly linearly to ~80 μm over the time for all operating conditions. In the interval from Day 7–56, the absolute roughness coefficients varied over time, increasing slightly. From Day 56–105, the relative and absolute roughness coefficients decreased, with a decrease of around 3–5 μm and 0.03–0.06, respectively. However, it is worth noting that the biofouling layer had a highly porous morphology at the top and a slight detachment of the biofouling layer from the membrane surface was clearly observed in the OCT image at the end of operation (Fig. 3g). This is a clear indication that during GDM filtration, the biofouling layer structures (i.e., roughness and porosity) experienced dynamic changes. The combined information from thickness, roughness, and porosity are important for elucidation of the biofouling layer morphology and to link this to the filtration performance.

The presence of eukaryotes (such as protists and metazoans) was illustrated by direct microscopic observation through the glass window of the filtration cell (i.e., the eukaryotes could be observed in the channel of the filtration cell or on the membrane surface). Fig. 5 shows examples of microscopic images of different eukaryotes of different sizes, shapes, and motility patterns. Flagellates, amoeboids and ciliates were frequently observed in the channel of the filtration cell. The movement of eukaryotes were observed along the surface of the biofouling layer, which may have caused the changes in the biofouling layer roughness and the internal structure. However, it is not clear whether the temperature and hydrostatic pressure had an influence on the eukaryotic diversity and quantity.

To further examine the biofouling layer morphology and microbial community structure, the membranes were removed from the filtration cells at Day 21 and Day 42. CLSM images (Fig. 6) revealed that the biofouling layer formed on the membranes displayed a high viability (almost no dead cells were observed). In addition to the open and heterogeneous structure of the biofouling layer, the existence of large and thick biomass mounds on the biofouling layer surface was also noticed. It has been previously reported that for the GDM process the presence of eukaryotes in the biofouling layer and their movement and predation behaviour resulted in a heterogeneous and porous biofilm on the membrane biofilm (Derlon et al., 2013, 2012; Kim et al., 2013). The mean thickness (H), biovolume (B), and porosity (P) of biofouling layers as calculated by IMARIS software are shown in Fig. 6. The mean thickness of the biofouling layer analyzed by the CLSM image was about 20–70% less than that of the OCT analysis. This may be because the loosely attached cake layers were partially removed during the pretreatment process of the CLSM sample. With extended filtration time, from 21 to 42 days, at a low temperature (21 ± 1 °C), the biovolume was constant (40 mbar) or increased (100 mbar) and the porosity decreased, which corresponds with the increasing fouling resistance (Fig. 2b). At a higher temperature (29 ± 1 °C), the biovolume reduced and porosity increased with the filtration time. This may be associated with a higher predation activity of the grazers (Derlon et al., 2013). However, the fouling resistance increased during this period of time (Fig. 2b). Possibly, more colloidal/dissolved organic substances were formed from the bacterial debris that became embedded in the openings of the biofilm (Kim et al., 2013).

The biofouling layer was carefully removed from the membrane surface and its DNA was extracted. Due to the

limited amount of eukaryotic DNA extracted from the biofouling layer, the analysis of eukaryote community compositions was not performed. The sequencing results of bacterial 16S rRNA gene (Fig. 7) indicate that the microbial community attached to the membrane was highly diversified and composed of approximately 600 OTUs, where each OTU represents one identity at the genus level (97% similarity). While most of the OTUs were detected at low abundance, some genera were found to be present at higher percentages (Fig. 7).

It has been reported that γ-proteobacteria in seawater are responsible for the major pioneering members in the formation of biofilms by adhesion to membrane surfaces (Bae et al., 2011). The relative abundances of γ-proteobacteria were calculated and slightly decreased with filtration time from Day 21–42 for all the operating conditions (at 21 ± 1 °C, 6–12% to ~5%; at 29 ± 1 °C, 11–12% to 7–8%). In this study, the dominant species in the biofilm seem to appear temperature and time dependent. For example, some species (e.g., *Verrucomicrobiales*) were present at 21 ± 1 °C, but absent at 29 ± 1 °C; while some species (e.g, *Myxococcales*, *Sphingomonadales*) existed at 29 ± 1 °C, but were not detected at 21 ± 1 °C. Significant shifts in the dominant microbial populations occurred from Day 21 to Day 42 under different hydrostatic pressures and temperatures. It was found that *Planctomycetales* significantly propagated in the biofouling layer within these 20 days for all the conditions. The abundances of *Verrucomicrobiales* (at

21 ± 1 °C), and *Myxococcales*/*Sphingomonadales* (at 29 ± 1 °C) in the biofouling layer tended to decrease with the filtration time. However, we cannot conclude whether the microbial community changes were related to their adaptation to the environments or to the predation behaviours of the eukaryotes.

3.3. GDM permeate quality

The characteristics of the seawater in the feed tanks and in the permeate-collected bottles were monitored regularly. The feed seawater had an average pH level of 7.6–7.7 and a conductivity value of 40.8–42.2 mS/cm. The DO in the feed tank was kept at approximately 3.3–3.5 mg/L (Table S1). It was found that the concentrations of the main cations in the feed and permeate seawater were very similar, which implies that the retention of cations by the membranes during the filtration process was negligible (Table S1 and S2 in the supplementary data). However, the turbidity of the permeate seawater (0.17 ± 0.03 NTU) was dramatically lower than that of the feed seawater (23.6 ± 2.0 NTU; Table 2), which suggests that the most of particulates and colloids were retained by the GDM process.

The organic substances (i.e., TOC, polysaccharides, TEP, biopolymers, humics, building blocks, low molecular weight compounds) in the feed and permeate seawater are presented in Table S1 and S2 respectively. Noticeably, at
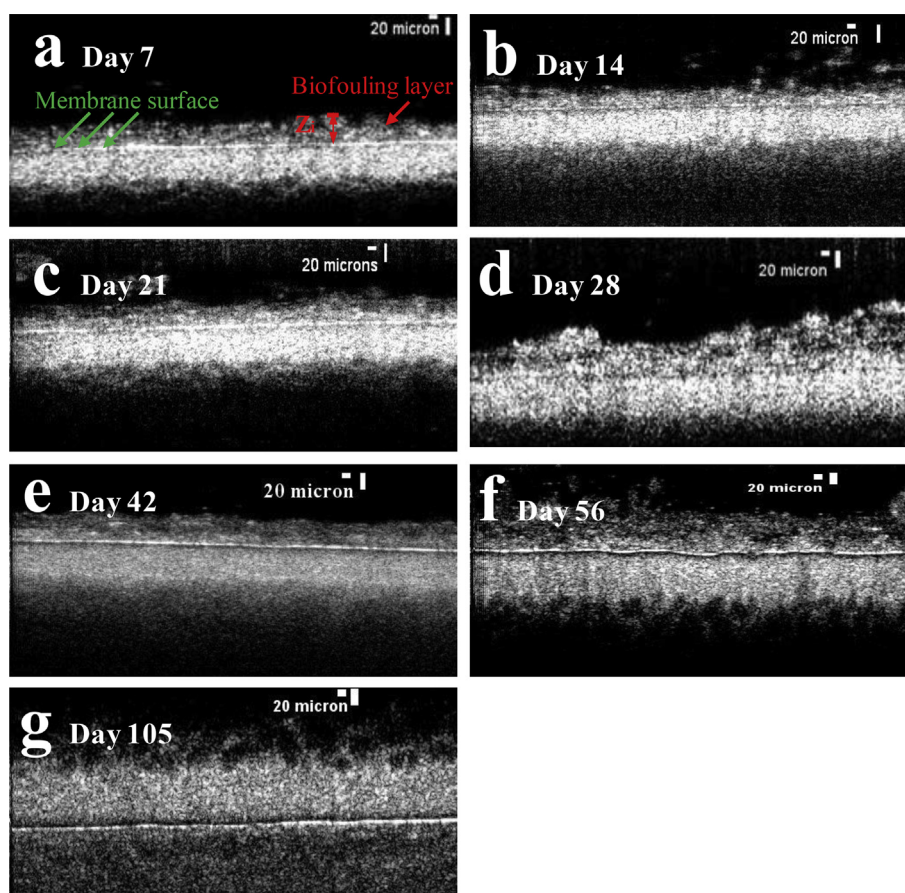

Fig. 3 – Typical OCT images showing the development of biofouling layer on the membrane with operation time (21 ± 1 °C, 40 mbar). The scale bars indicating the horizontal and vertical dimension were presented.

different temperatures, the amounts and types of organic substances in the feed tank were dissimilar although the same fresh feed seawater was added into the storage tank. Due to the long hydraulic retention time of the system, it took almost 2—5 days to completely renew the seawater in the feed tank. Under such conditions, the feed tank performed as a bioreactor, in which carbon degradation and fixation occurred before it was fed into the membrane filtration cells.

Surprisingly, TOC levels in the permeate (4.5—5.4 mg/L) were slightly higher or close to the levels observed in the feed (4.1—4.2 mg/L). In this study, the filtration process was
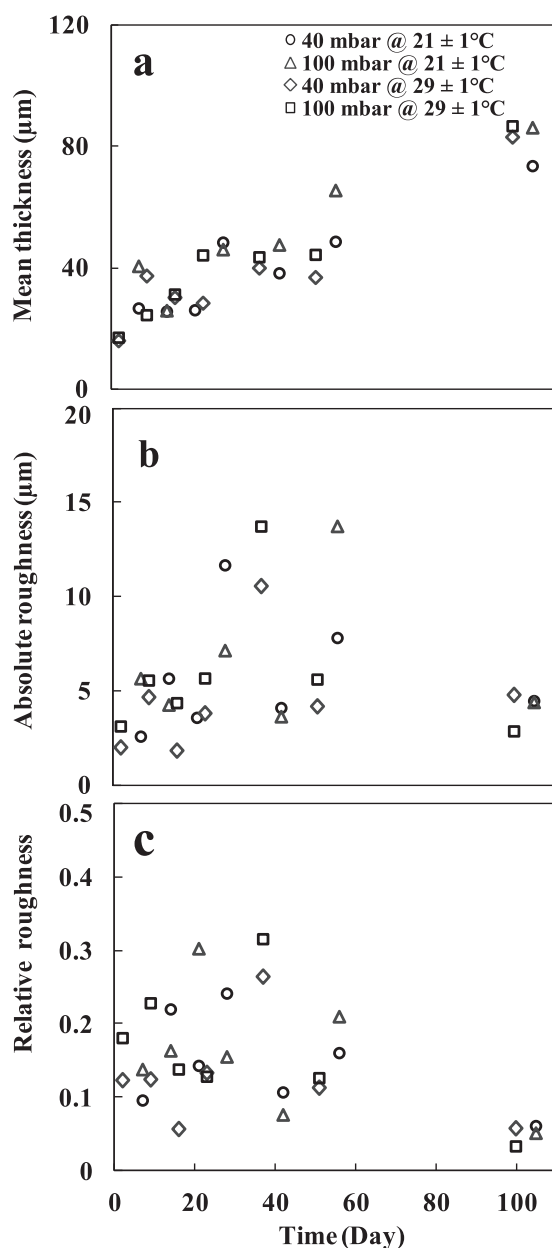
performed in the dark in order to prevent carbon fixation via photosynthesis. However, activities such as feeding seawater into the tank, taking samples, and changing tubing, etc. would have exposed the setup to light for a short time each day. In addition, some microbial species may use other inorganic carbon or energy sources (e.g., hydrogen sulphide) (Kleiner et al., 2012).

At a higher operational hydrostatic pressure, TOC levels in the permeate were lower than when the system was operated at a lower pressure. It is well known that fouling layers can act as a secondary membrane to retain some organic matter. As presented above, the membranes operated at the higher hydrostatic pressure (100 mbar) had a fouling layer with higher resistance (Fig. 2b and Table 1), which may have facilitated the retention of organic substances on the feed side. Similar to the TOC concentration, the amount of TEP in the permeate was higher than that in the feed. As reported by Discart et al. (Discart et al., 2014, 2015), the increases of TOC and TEP in the permeate may be associated with the excreted matters of microalgae, which may propagate in the filtration cells. Furthermore, the polysaccharide concentration in the permeate was approximately 0.23—0.38 mg/L, which is lower than in the feed (0.44—0.51 mg/L).

LC-OCD-OND was employed to quantify dissolved organic substances such as biopolymers, humics, building blocks and low molecular weight organic substances (including acid and neutral substances) in the feed and permeate seawater (Figs. 8 and 9; Table S1 and S2), which were separated on the basis of size and chemical functions (Huber et al., 2011). The biopolymer fraction is composed of hydrophilic, non-ionic substances with a high molecular weight. Building blocks are considered to be breakdown products of humic substances, which reflect humic-like material with lower molecular weight (Huber et al., 2011). The dissolved organic carbon content measured by LC-OCD-OND was approximately 2.2—2.7 mg/L (the sample was pretreated by a 0.45 μm filter), which indicates that about 40% of the organic material was readily removed by the 0.45 μm filter due to either size exclusion or adsorption effects (i.e., the amount of organic material that is available to readily build a fouling layer on the filter).

At a temperature of 21 ± 1 °C, the concentration of biopolymers and building blocks in the permeate (112—125 μg/L and 199—237 μg/L respectively) were lower than in the feed (167 μg/L and 371 μg/L respectively). However, at 29 ± 1 °C, the permeate had slightly increased concentrations of biopolymers (386—427 μg/L) and building blocks (337—368 μg/L) than the feed (339 μg/L and 278 μg/L respectively). There was almost no difference in humics in the feed and permeate at any of the operating conditions. However, the low molecular weight compounds in the permeate (1282—1513 μg/L and 2404—2677 μg/L at 21 ± 1 °C and 29 ± 1 °C respectively) were approximately 2—2.5 fold those in the feed (667 and 1139 μg/L at 21 ± 1 °C and 29 ± 1 °C respectively).

Furthermore, the RO fouling potential of feed and permeate seawater were assessed based on the silt density index (SDI) and modified fouling index (MFI). As shown in Table 2, the SDI_5 and $MFI_{0.45}$ of the permeate seawater were 8.9 ± 0.5 and 21 ± 4 s/L^2, which were significantly lower than those of the feed seawater (14.8 ± 0.7 and 876 ± 6 s/L^2).

Fig. 4 — **Mean biofouling layer thickness (a), absolute (b) and relative roughness (c) of biofouling layers developed on the membranes operated under different conditions. These physical parameters were calculated by analyzing OCT images.**

4.   Discussion

4.1.   Membrane fouling during GDM process

Previous studies have demonstrated that the flux tends to stabilize during gravity-driven dead-end UF of different types of surface waters and diluted wastewaters (Peter-Varbanets et al., 2012, 2010, 2011). In this study, flux stabilization was also achieved at all conditions tested when seawater was used as feed water. This provides evidence that low-energy gravity-driven UF processes to pre-treat seawater as feed for reverse osmosis (SWRO) is possible.

A four-stage flux profile was observed in this study using a dead-end filtration mode, almost regardless of the applied temperature and hydrostatic pressure (Fig. 2a). Previous studies on fouling mechanisms of dead-end filtration under
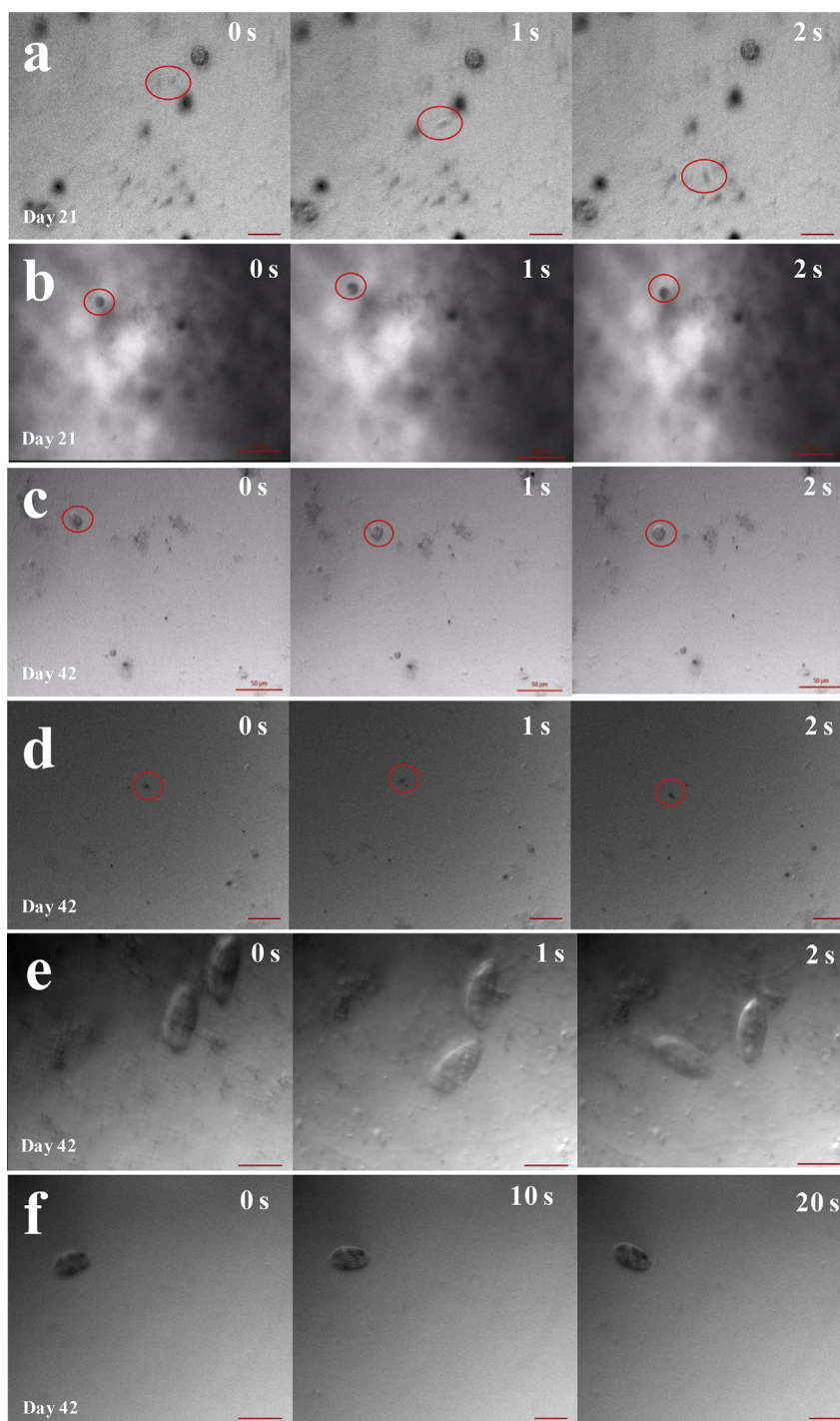

Fig. 5 – Observation of eukaryotic organisms on the biofouling layer by the optical microscope at Day 21 and Day 42 (200× magnification; the scale bar represents 50 μm).

constant pressure have illustrated four classic filtration models based on the following equation (Hermia, 1985):

$$\frac{d^2t}{dV^2} = k\left(\frac{dt}{dV}\right)^n \tag{8}$$

where t is the filtration time and V is the total filtered volume. The exponent n characterizes the filtration model, with $n = 0$ for cake filtration ($t/V = aV + b$), $n = 1$ for intermediate blocking ($1/J = at + b$), $n = 3/2$ for pore constriction (i.e., standard blocking, $t/V = at + b$), and $n = 2$ for complete pore blocking ($-\ln (J/J_0) = at + b$) (Ho and Zydney, 2000; Ye et al., 2005).

The experimental data have been tested with the linearized forms of the four fouling models. For all the conditions and throughout the duration of the runs, the pore constriction and cake filtration models were found to describe the experimental data the best, both in a two-stage profile (Fig. 10). During the initial filtration period, the potential foulants in the feed seawater directly interacted with the membrane, which either blocked pores or accumulated on the membrane surface. In view of the limited thickness of cake layer in the initial filtration period (Figs. 3 and 4), the rapid flux decline (Fig. 2, Phase I) can probably be mainly attributed to the loss of effective membrane pore volume (i.e., pore constriction was predominant). This could explain that the hydrostatic pressure and temperature had negligible effects on permeate flux at the early stage of filtration. Once the fully-covered biofouling layers reached a certain thickness, further flux variation (Phase II and III) and stabilization (Phase IV) could be linked to the biofouling layer structure changes (i.e., cake filtration was predominant). Phases II, III, and IV were more sensitive to temperature and pressure variation.

In addition, unexpectedly, the transition from pore blocking to cake filtration occurred at almost the same time for the membranes operated at different hydrostatic pressures (Fig. 10). Such a phenomenon is possibly related to the combined effects of the filtration situation and eukaryotic predation. Obviously, more seawater was filtered under a higher hydrostatic pressure (100 mbar) at the same temperature (Fig. 10b). Thus, more rejected foulants were expected to be accumulated in the membrane pores or on the membrane surface. Meanwhile, the higher driving force tended to compact the formed cake layer. These factors could accelerate the transition of pore blocking to cake filtration at a higher hydrostatic pressure. On the other hand, more eukaryotic organisms could also be retained in the filtration cell when more water was filtered at a higher hydrostatic pressure. Their
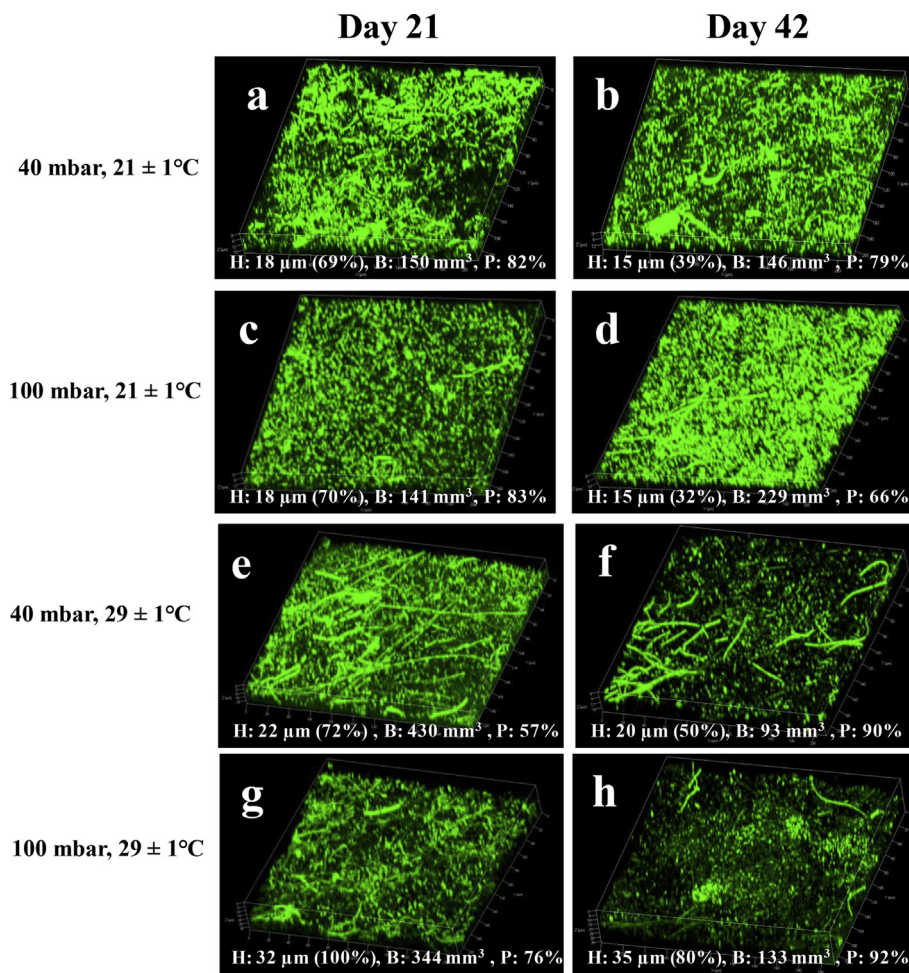

Fig. 6 – Biofouling layer development on the membranes taken by CLSM. H, B, and P represent the mean thickness, biovolume, and porosity of biofouling layer respectively. The number in the parentheses is the calculated ratio of the measured biofouling layer thickness by CLSM to the measured biofouling layer thickness by OCT.
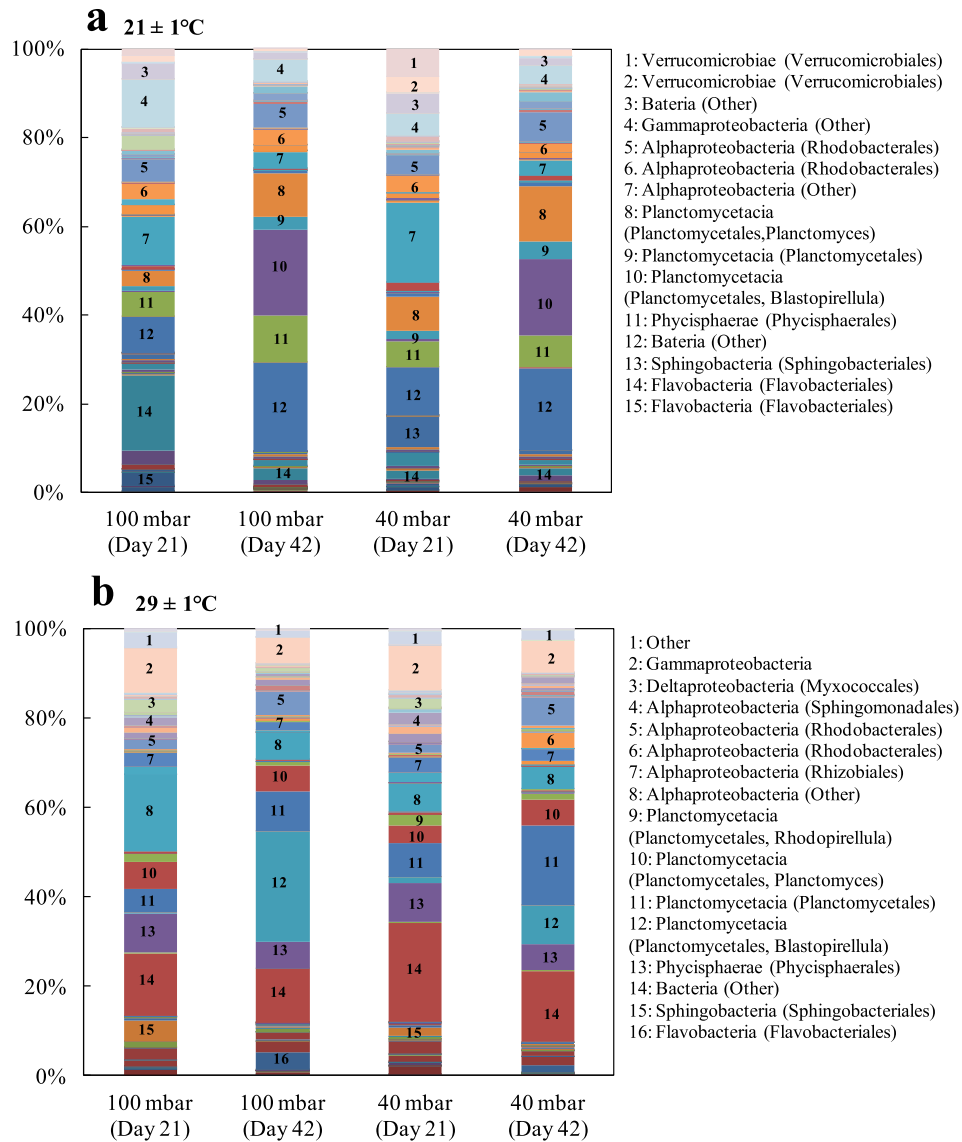
Fig. 7 – The changes of biofouling layer microbial community with filtration time at different operating conditions.

predation could increase the porosity/roughness of the formed cake layers (which will be illustrated in the following section 4.2), as a result, delaying the transition of pore blocking to cake filtration. It appears these competing effects balanced each other.

4.2. The association of dynamic cake layer morphologies with flux development

During the period from Day 7 to the end of the filtration at Day 105, OCT images demonstrated that the biofouling layer thickness increased nearly linearly with filtration time (Figs. 3

and 4; Figs. S2–S4). It is not surprising that during dead-end filtration all retained material is deposited on the membrane, resulting in an increase of biofouling layer thickness. However, the flux or fouling resistance did not decrease linearly, indeed, the flux and fouling resistance experienced three stages: flux slightly increased, then slowly decreased and finally stabilized at a constant level (Fig. 2b). As discussed in section 4.1, cake layer fouling was predominant during this period of time, with resistances determined by the biofouling layer thickness and structural parameters according to the Carman–Kozeny equation and Darcy's Law:

$$R_{\text{biofilm cake layer}} = \frac{75(1-\varepsilon)^2}{2\varepsilon^3 \alpha^2} H \qquad (9)$$

Where ε (dimensionless) is the biofouling layer porosity, α (m) is the characteristic radius of the particles forming the cake layer, and H (m) corresponds to the thickness of the biofouling layer (Derlon et al., 2012; Katsoufidou et al., 2005). Thus, the combined effects of the biofouling layer thickness and

Table 2 – Comparison of SDI$_5$, MFI$_{0.45}$ and turbidity of the feed and permeate seawater (21 ± 1 °C) (n = 2).

	SDI$_5$	MFI$_{0.45}$ (s/L^2)	Turbidity (NTU)
Feed seawater	14.8 ± 0.1	876 ± 6	23.6 ± 2.0
Permeate seawater	8.9 ± 1.7	21 ± 4	0.17 ± 0.03

structure determined the flux development profile patterns. The non-linear correlation between fouling resistance and biofouling layer thickness and porosity (Table S3) implies that the attached microbial floc size dynamically varied with the filtration time.

The time-dependent changes in the structure of the biofouling layer may be due to a few factors. Firstly, in the few previous studies, researchers have explained that bacterial activity and predation are capable of altering biofilm morphology and affecting the spatial arrangement of the biofouling layer (Bohme et al., 2009; Derlon et al., 2012; Peter-Varbanets et al., 2010). In this study, as illustrated by the microscopic and CLSM images, different types of the eukaryotic organisms were present on the membrane surface (Fig. 5) as well as inside of the biofouling layer (Fig. 6). In addition, larger roughness coefficients were observed at the flux

fluctuation stages (Phase II and III; i.e., higher flux) than those at the flux stabilization stage (Phase IV; i.e., lower flux). Thus, the movement of the eukaryotes and predation of the bacteria by the eukaryotic organisms in the biofouling layer resulted in a more heterogeneous structure. Secondly, the biofouling layer had a diverse microbial community composition and the dominant microbial species shifted over time (Fig. 7). The changes in microbial community structure indicate that some microbial species propagated, while the abundance of other species decreased, which may have lead to different biofouling layer structures (e.g., different microbial floc size). Thirdly, the predation activity generates waste material, i.e., bacterial debris. Such colloidal/dissolved organic substances could have occupied void volume in the biofilm and reduce the porosity (Kim et al., 2013).
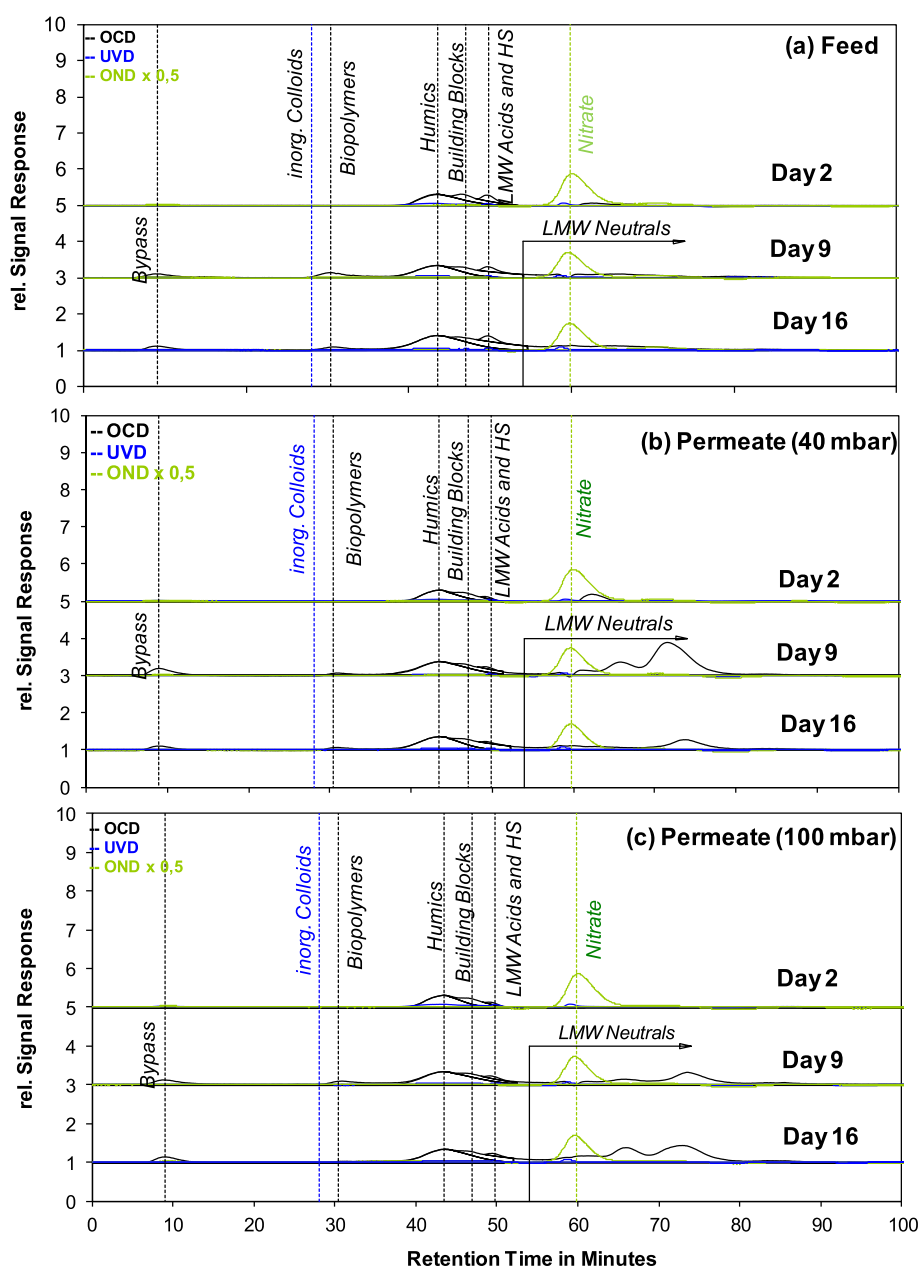

Fig. 8 — LC-OCD of feed and permeate samples taken from the experiments at a temperature of 21 ± 1 °C.

Although the effects of temperature and hydrostatic pressure on the dynamic biofouling layer thickness and roughness coefficients showed no conclusive trends (Fig. 4), their influences on the permeate flux (also the flux corrected to 20 °C) and fouling resistance followed the same pattern during cake layer fouling at the predominant stage (Fig. 2 and Table 1). In particular, membrane filtration at a higher temperature (29 ± 1 °C) achieved improved flux with lower fouling resistance; and at a higher hydrostatic pressure (100 mbar), a higher flux with higher fouling resistance was observed. It should be noted that the feed seawater was sampled from a typical tropical environment (seawater temperature during
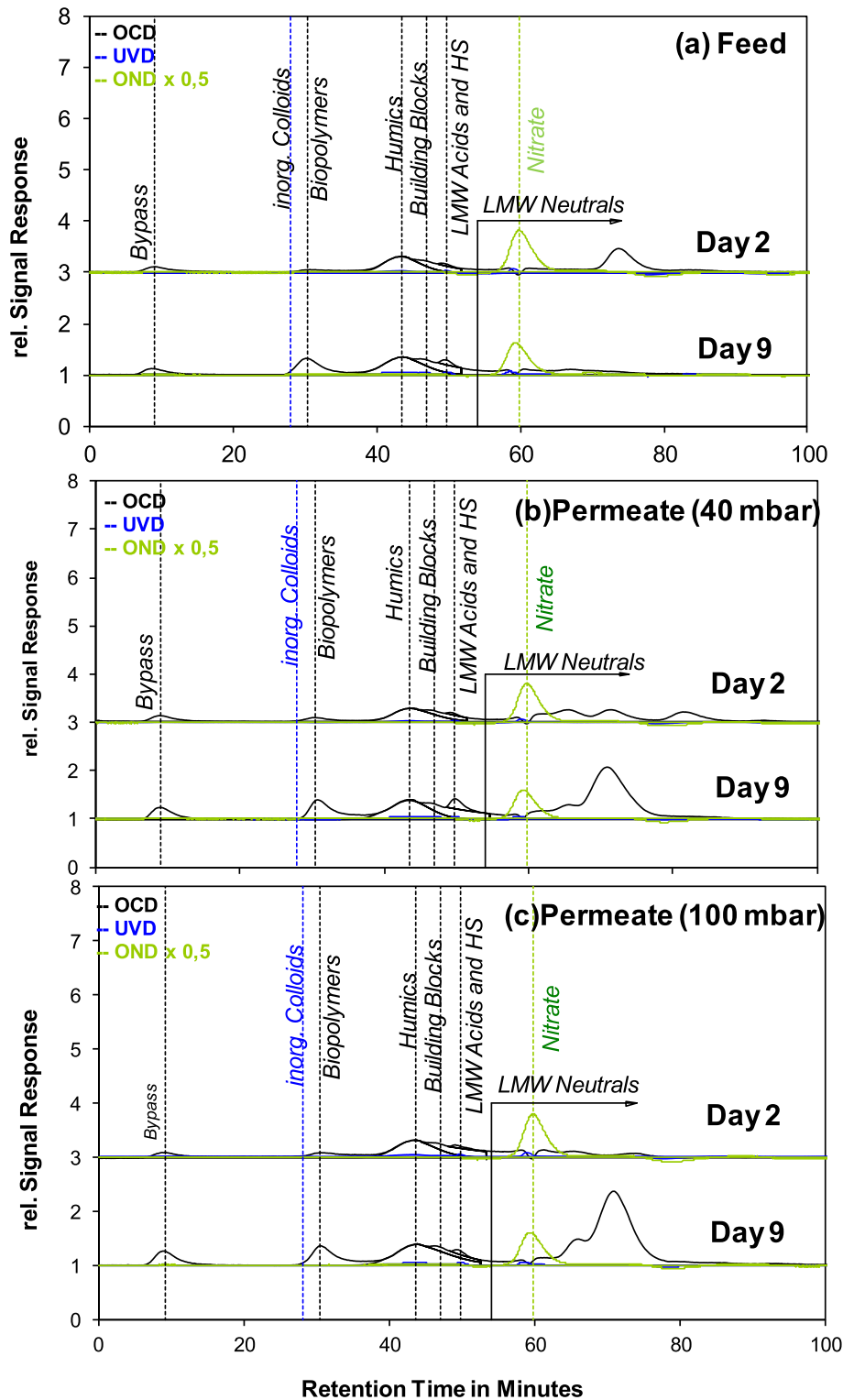

Fig. 9 – LC-OCD of feed and permeate samples taken from the experiments at a temperature of 29 ± 1 °C.

Sep to Dec is approximately 29 °C (http://www.seatemperature.org/asia/singapore/singapore.htm)). It is possible that the microbial and eukaryotic organisms are more active at 29 than at 21 °C. However, bacterial growth may be restricted by the limited organic carbon concentration. Thus, higher predation activity may lead to the formation of a biofouling layer with more porosity (Fig. 6), i.e., less resistance. On the other hand, at different hydrostatic pressures, although the biofouling layers had similar thickness, the resistance of the fouled membrane increased with elevated hydrostatic pressure. This is attributed to the fact that the higher hydrostatic pressure can lead to compaction of the cake layers.

4.3. Implications of the GDM process

In this study, the GDM process efficiently removed particulates and colloidal matter (~99% removal efficiency as assessed by turbidity). The RO fouling potential (as SDI or MFI) of the seawater was dramatically decreased after being treated by the GDM process. However, it was not anticipated that the organic matter in the permeate would be higher than

or comparable to that of the feed, and in particular, the high abundance of low molecular weight substances in the permeate was surprising (Tables S1 and S2). This phenomenon is likely to be associated with the carbon fixation activities of the microbial biofilm. Dissolved organic solutes that pass through the UF membrane may be a problem for RO, as it can lead to organic fouling due to surface adsorption, or biofouling due to growth of bacteria. Therefore, it will be necessary to investigate the effect of these organics on RO fouling and to explore ways to mitigate their effect (Pearce, 2008). Recently, researchers emphasized that the assimilable organic carbon (AOC, a fraction of "labile" or "bio-available" DOC) should be considered to be a more accurate parameter to predict biofouling in RO systems (Naidu et al., 2013). Thus, in future work, the AOC profile in the GDM system will be measured to assess further the potential of GDM as an RO pretreatment strategy.

To further improve the permeate quality of GDM filtration, combining the advantages of conventional processes with GDM filtration system is proposed for future study. Recently, Naidu et al. (2013) elucidated that approximately 41% of low molecular weight organic compounds, 90% AOC and 84% TEP could be removed by granular activated carbon (GAC) biofilters in a deep-bed biofilter system. It is anticipated that such a hybrid carrier biofilm-submerged GDM could provide an effective low energy pretreatment for RO feed water. The GDM process and hybrid configurations need to be optimized in terms of energy consumption, maintenance, productivity and footprint.
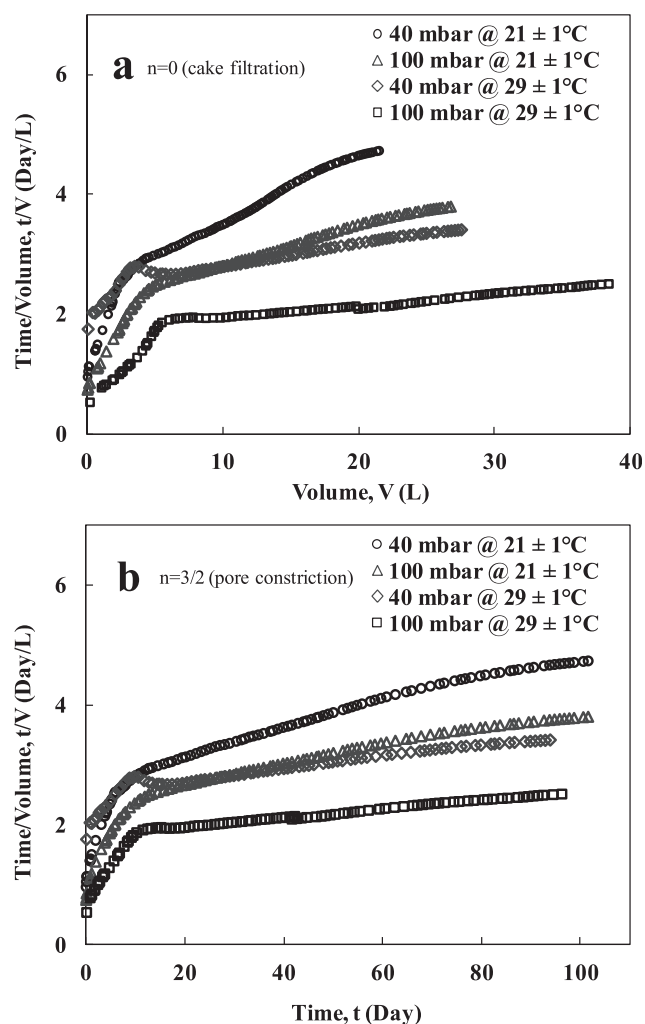
5. Conclusions

The potential of gravity-driven membrane (GDM) filtration as a pretreatment for the seawater RO process was investigated in this study. Filtration experiments with tropical seawater were performed at temperatures of 21 ± 1 and 29 ± 1 °C, at hydrostatic pressures of 40 and 100 mbar. The following conclusions can be drawn:

(1) The permeate flux and fouling resistance experienced a four-stage trend at all operating conditions: flux was dramatically decreased followed by a slight jump, then slowly decreased, finally stabilized at a constant level.

(2) At the early stage of filtration, the hydrostatic pressure and temperature had negligible effects on permeate flux due to the predominant pore constriction fouling mechanism. After that, cake layer fouling played a dominant role. Both higher hydrostatic pressure and temperature improved permeate flux.

(3) During the predominant cake layer fouling period, the combined effect of biofouling layer thickness and structure determined the dynamic developments of permeate flux and fouling resistance. The biofouling layer thickness increased linearly with filtration time, but biofouling layer porosity and foulant dimension fluctuated over time. The alterations of biofouling layer structure were associated with (1) movement and predation behaviours of the eukaryotic organisms in the biofouling layer; (2) the bacterial debris generated by

Fig. 10 – The relationship between the experimental t/V data with filtration volume (a) and filtration time (b).

predation activity of eukaryotes; (3) bacterial community shifts.

(4) The GDM process could effectively remove the particulates and colloidal foulants from the feed seawater, which led to decreased RO fouling potential. However, the low molecular weight substances in the permeate were unexpectedly higher than those in the feed. To further improve the permeate quality of GDM filtration, it is proposed to combine the GDM filtration with additional low energy biofilm contact systems.

Acknowledgements

Appendix A. Supplementary data

Supplementary data related to this article can be found at http://dx.doi.org/10.1016/j.watres.2014.12.001.

REFERENCES

Akhondi, E., Wicaksana, F., Fane, A.G., 2014. Evaluation of fouling deposition, fouling reversibility and energy consumption of submerged hollow fiber membrane systems with periodic backwash. J. Membr. Sci. 452, 319–331. http://dx.doi.org/10.1016/j.memsci.2013.10.031.

Bae, H., Kim, H., Jeong, S., Lee, S., 2011. Changes in the relative abundance of biofilm-forming bacteria by conventional sand-filtration and microfiltration as pretreatments for seawater reverse osmosis desalination. Desalination 273 (2–3), 258–266. http://dx.doi.org/10.1016/j.desal.2010.12.030.

Boerlage, S.F.E., Kennedy, M.D., Aniye, M.P., Abogrean, E.M., Galjaard, G., Schippers, J.C., 1998. Monitoring particulate fouling in membrane systems. Desalination 118 (1–3), 131–142.

Bohme, A., Risse-Buhl, U., Kusel, K., 2009. Protists with different feeding modes change biofilm morphology. FEMS Microbiol. Ecol. 69 (2), 158–169. http://dx.doi.org/10.1111/j.1574-6941.2009.00710.x.

Bonnelye, W., Sanz, M.A., Durand, J.P., Plasse, L., Gueguen, F., Mazounie, P., 2004. Reverse osmosis on open intake seawater: pre-treatment strategy. Desalination 167 (1–3), 191–200. http://dx.doi.org/10.1016/j.desal.2004.06.128.

Derlon, N., Koch, N., Eugster, B., Posch, T., Pernthaler, J., Pronk, W., Morgenroth, E., 2013. Activity of metazoa governs biofilm structure formation and enhances permeate flux during Gravity-Driven Membrane (GDM) filtration. Water Res. 47 (6), 2085–2095. http://dx.doi.org/10.1016/j.watres.2013.01.033.

Derlon, N., Peter-Varbanets, M., Scheidegger, A., Pronk, W., Morgenroth, E., 2012. Predation influences the structure of biofilm developed on ultrafiltration membranes. Water Res. 46 (10), 3323–3333. http://dx.doi.org/10.1016/j.watres.2012.03.031.

Discart, V., Bilad, M.R., Marbelia, L., Vankelecom, I.F.J., 2014. Impact of changes in broth composition on Chlorella vulgaris cultivation in a membrane photobioreactor (MPBR) with permeate recycle. Bioresour. Technol. 152, 321–328. http://dx.doi.org/10.1016/j.biortech.2013.11.019.

Discart, V., Bilad, M.R., Vankelecom, I.F.J., 2015. Critical evaluation of the determination methods for transparent exopolymer particles, agents of membrane fouling. Crit. Rev. Environ. Sci. Technol. 45 (2), 167–192. http://dx.doi.org/10.1080/10643389.2013.829982.

Dubois, M., Gilles, K., Hamilton, J.K., Rebers, P.A., Smith, F., 1956. Colorimetric method for the determination of sugars and related substances. Anal. Chem. 28, 350–356.

Elimelech, M., Phillip, W.A., 2011. The future of seawater desalination: energy, technology, and the environment. Science 333 (6043), 712–717. http://dx.doi.org/10.1126/science.1200488.

EPA, 2005. Membrane Filtration Guidance Manual (EPA 815-R-06-009). United States Environmental Protection Agency, Office of Ground Water and Drinking Water.

Hermia, J., 1985. Blocking filtration – application to non-newtonian fluids. In: Rushton, A. (Ed.), Mathematical Models and Design Methods in Solid-liquid Separation. Martinus Nijhoff Publishers, Dordrecht.

Ho, C.C., Zydney, A.L., 2000. A combined pore blockage and cake filtration model for protein fouling during microfiltration. J. Colloid Interface Sci. 232 (2), 389–399. http://dx.doi.org/10.1006/jcis.2000.7231. http://www.seatemperature.org/asia/singapore/singapore.htm.

Huang, H.O., Cho, H., Schwab, K., Jacangelo, J.G., 2011. Effects of feedwater pretreatment on the removal of organic microconstituents by a low fouling reverse osmosis membrane. Desalination 281, 446–454. http://dx.doi.org/10.1016/j.desal.2011.08.018.

Huber, S.A., Balz, A., Abert, M., Pronk, W., 2011. Characterisation of aquatic humic and non-humic matter with size-exclusion chromatography – organic carbon detection – organic nitrogen detection (LC-OCD-OND). Water Res. 45 (2), 879–885. http://dx.doi.org/10.1016/j.watres.2010.09.023.

Katsoufidou, K., Yiantsios, S.G., Karabelas, A.J., 2005. A study of ultrafiltration membrane fouling by humic acids and flux recovery by backwashing: experiments and modeling. J. Membr. Sci. 266 (1–2), 40–50. http://dx.doi.org/10.1016/j.memsci.2005.05.009.

Kim, E.H., Dwidar, M., Mitchell, R.J., Kwon, Y.N., 2013. Assessing the effects of bacterial predation on membrane biofouling. Water Res. 47 (16), 6024–6032. http://dx.doi.org/10.1016/j.watres.2013.07.023.

Kleiner, M., Petersen, J.M., Dubilier, N., 2012. Convergent and divergent evolution of metabolism in sulfur-oxidizing symbionts and the role of horizontal gene transfer. Curr. Opin. Microbiol. 15 (5), 621–631. http://dx.doi.org/10.1016/j.mlb.2012.09.003.

Knops, F., van Hoof, S., Futselaar, H., Broens, L., 2007. Economic evaluation of a new ultrafiltration membrane for pretreatment of seawater reverse osmosis. Desalination 203 (1–3), 300–306. http://dx.doi.org/10.1016/j.desal.2006.04.013.

Liu, L., Gardecki, J.A., Nadkarni, S.K., Toussaint, J.D., Yagi, Y., Bouma, B.E., Tearney, G.J., 2011. Imaging the subcellular structure of human coronary atherosclerosis using micro-optical coherence tomography. Nat. Med. 17 (8), 1010–1014.

Naidu, G., Jeong, S., Vigneswaran, S., Rice, S.A., 2013. Microbial activity in biofilter used as a pretreatment for seawater desalination. Desalination 309, 254–260. http://dx.doi.org/10.1016/j.desal.2012.10.016.

Passow, U., Alldredge, A.L., 1995. A dye-binding assay for the spectrophotometric measurement of transparent exopolymer particles (TEP). Limnol. Oceanogr. 40 (7), 1326–1335.

Pearce, G.K., 2008. UF/MF pre-treatment to RO in seawater and wastewater reuse applications: a comparison of energy costs. Desalination 222 (1–3), 66–73. http://dx.doi.org/10.1016/j.desa1.2007.05.029.

Peter-Varbanets, M., Gujer, W., Pronk, W., 2012. Intermittent operation of ultra-low pressure ultrafiltration for decentralized drinking water treatment. Water Res. 46 (10), 3272–3282.

Peter-Varbanets, M., Hammes, F., Vital, M., Pronk, W., 2010. Stabilization of flux during dead-end ultra-low pressure ultrafiltration. Water Res. 44 (12), 3607–3616. http://dx.doi.org/10.1016/j.watres.2010.04.020.

Peter-Varbanets, M., Margot, J., Traber, J., Pronk, W., 2011. Mechanisms of membrane fouling during ultra-low pressure ultrafiltration. J. Membr. Sci. 377 (1–2), 42–53. http://dx.doi.org/10.1016/j.memsci.2011.03.029.

Schippers, J.C., Verdouw, J., 1980. Modified fouling index, a method of determining the fouling characteristics of water. Desalination 32 (1–3), 137–148. http://dx.doi.org/10.1016/S0011-9164(00)86014-2.

Sutzkover-Gutman, I., Hasson, D., 2010. Feed water pretreatment for desalination plants. Desalination 264 (3), 289–296. http://dx.doi.org/10.1016/j.desal.2010.07.014.

Voutchkov, N., 2010. Considerations for selection of seawater filtration pretreatment system. Desalination 261 (3), 354–364. http://dx.doi.org/10.1016/j.desa1.2010.07.002.

Ye, Y., Le Clech, P., Chen, V., Fane, A.G., Jefferson, B., 2005. Fouling mechanisms of alginate solutions as model extracellular polymeric substances. Desalination 175 (1), 7–20. http://dx.doi.org/10.1016/j.desal.2004.09.019.